Evolutionary rewiring of host metabolism and interferon signalling by SARS-CoV-2 variants

Riaz-Ali Somji[1†], Jonathan C Brown[2†], Shahid Rowles-Khalid[3,4], Tukur Abdullahi[1], Dongsheng Luo[1], Natalie Barthel[5], Michael Mülleder[6], Markus Ralser[5], Wendy S Barclay[2‡], Charalampos Rallis[7‡], Efstathios S Giotis[1,2‡*]

[1]School of Life Sciences, University of Essex, Colchester, UK

[2]Department of Infectious Diseases, School of Medicine, Imperial College London, London, UK

[3]EGA Institute for Women's Health, Faculty of Population Health Sciences and Department of Mathematics, University College London, London, UK

[4]Department of Metabolism, Digestion and Reproduction, Imperial College London, London, UK

[5]Department of Biochemistry, Charité - Universitätsmedizin Berlin, Berlin, Germany

[6]Core Facility High Throughput Mass Spectrometry, Charité – Universitätsmedizin. Berlin, Germany

[7]Research Centre for Molecular Cell Biology, School of Biological and Behavioural Sciences, Queen Mary, University of London, London, UK

[†]Joint first authors

[‡]Corresponding authors with emails.

*Lead contact

Summary

SARS-CoV-2 variants differ in transmissibility and immune evasion, but their effects on host-cell metabolism and signalling remain less defined. Using integrated transcriptomic, phosphoproteomic, and amino acid profiling in primary nasal epithelial cells, we compared early and late host responses to pre-Omicron variants (Alpha, Beta), Delta, and Omicron subvariants (BA.1, BA.5). Pre-Omicron strains broadly suppressed antiviral interferon-stimulated gene expression and reprogrammed metabolism by reducing mitochondrial oxidative phosphorylation and β-oxidation. Delta infection was associated with extensive transcriptional and metabolic remodelling, characterised by activation of stress- and growth-related kinases and selective retention of biosynthetic amino acids, consistent with a host response to stress and viral modulation of interferon-associated signalling. In contrast, Omicron infection elicited a more restrained response dominated by cytokine and survival pathways, with limited metabolic activation and interferon suppression. Together, these findings suggest SARS-CoV-2 has progressively evolved toward a strategy that maintains efficient upper-airway replication while minimising epithelial stress and inflammation.

Keywords: SARS-CoV-2 variants, interferon-stimulated genes, metabolic reprogramming, nasal epithelial cells, host-pathogen interactions

Introduction

SARS-CoV-2, the causative agent of COVID-19, has evolved into multiple variants with distinct transmissibility, immune evasion capacity, and associated disease severity. The successive waves of Variants of Concern (VOCs), including Alpha (PANGO lineage B.1.1.7), Beta (B.1.351), Delta (B.1.617.2/AY sublineages), and the many Omicron sublineages (B.1.1.529/BA sublineages, such as BA.1, BA.2, and BA.5), exhibit distinct phenotypic characteristics and transmission advantages over preceding variants. These advantages are largely driven by genetic changes in the viral genome, particularly in the spike protein, which enhanced receptor binding affinity and immune escape (Carabelli *et al*., 2023; Harvey *et al.*, 2021; Liu and Rocklov, 2021). Additionally, VOCs exhibit varying capacities to suppress innate immune responses, a key determinant of early viral control and disease progression (Carabelli *et al.*, 2023; Harvey *et al.*, 2021; Laine *et al.*, 2022; Reuschl *et al*., 2024).

The nasal epithelium serves as the primary entry site for SARS-CoV-2 infection and plays a critical role in shaping early host responses (Shi *et al.*, 2024; Sungnak *et al.*, 2020). Nasal epithelial cells (NECs) serve as both the primary site of viral entry and replication and as an essential frontline of antiviral immunity, producing interferons (IFNs), a family of cytokines that coordinate antiviral defence (Desmyter *et al*., 1968; Sposito *et al.*, 2021). Type I (e.g., IFN-α and IFN-β) and type III (e.g., IFN-λ) interferons bind to their respective receptors on infected and neighbouring cells, triggering the Janus kinase/signal transducer and activator of transcription (JAK-STAT) pathway. Type II interferon (IFN-γ), primarily derived from immune effector cells, complements these pathways by amplifying antiviral and immunomodulatory responses once immune infiltration occurs. This leads to the induction of hundreds of interferon-stimulated genes (ISGs), which act collectively to inhibit viral replication, degrade viral RNA, and enhance antigen presentation (Park and Iwasaki, 2020; Schneider *et al*., 2014).

68 SARS-CoV-2 has evolved multiple strategies to suppress these IFN responses, thereby evading
69 early immune detection and promoting viral persistence (Carabelli *et al.*, 2023; V'Kovski *et al.*,
70 2021; Yuen *et al.*, 2020). The Alpha and Beta strains inhibit IFN production more effectively
71 than earlier reference strains (Gori Savellini *et al.*, 2023; Rajah *et al.*, 2021). Delta, in contrast,
72 displays enhanced replication efficiency and greater host immune antagonism, leading to
73 higher viral loads and increased disease severity (Liu and Rocklov, 2021; Rajah *et al.*, 2021). In
74 comparison, several studies suggest that Omicron subvariants exhibit a reduced interaction
75 with the interferon response, although some evidence indicates a delayed yet stronger
76 induction of ISGs (Gori Savellini *et al.*, 2023; Laine *et al.*, 2022; Shi *et al.*, 2024). Collectively,
77 these findings suggest that each variant has evolved unique strategies to modulate IFN
78 signalling and evade early antiviral defenses.
79 Among the emerging variants, Omicron variants remain globally dominant, as they rapidly
80 displaced previous VOCs, through successive waves of transmission. Unlike earlier SARS-CoV-
81 2 variants, Omicrons show an increased preference for the upper airways and a reduced
82 transition to the lower respiratory tract (Shi *et al.*, 2024). Studies suggest that mutations in
83 the Omicron spike protein enhance viral entry into nasal epithelial cells, enabling evasion of
84 both constitutive and interferon-induced antiviral factors that normally limit SARS-CoV-2
85 entry following attachment (Gori Savellini *et al.*, 2023; Reuschl *et al.*, 2024; Shi *et al.*, 2024).
86 In contrast to previous variants that predominantly rely on serine transmembrane proteases
87 for host cell entry, Omicron strains preferentially use cysteine proteases cathepsin B (CatB)
88 and cathepsin L (CatL) to catalyse endosomal membrane fusion, possibly providing an
89 advantage in nasal epithelial infection and potentially contributing to their increased
90 respiratory transmissibility (Giotis *et al.*, 2022; Leach *et al.*, 2021; Shi *et al.*, 2024). These

91 adaptations in entry mechanisms and tissue tropism raise important questions about how
92 variant-specific traits impact downstream host cellular responses.
93 While extensive research on VOCs has focused on spike protein mutations and their role in
94 enhancing viral entry and immune evasion, much less is known about how these variants
95 differentially reprogram host cell metabolism and signalling to optimise replication and
96 immune escape. Viruses such as Influenza A, Dengue, HBV, HIV and others typically hijack host
97 metabolic networks to create an environment conducive to replication, altering energy
98 production, amino acid biosynthesis, and lipid metabolism to support viral genome
99 replication, protein synthesis, and virion assembly (Allen *et al.*, 2022; Chan *et al.*, 2009; Liu *et*
100 *al.*, 2020; Long *et al*., 2016; Polcicova *et al*., 2020; Ritter *et al*., 2010; Singh *et al.*, 2020; Thaker
101 *et al.*, 2019). Current understanding of SARS-CoV-2 metabolic reprogramming largely derives
102 from studies on early variants**,** which have shown that the virus targets key pathways such as
103 glycolysis, the tricarboxylic acid (TCA) cycle, and the pentose phosphate pathway (PPP) to
104 meet biosynthetic and redox demands (Codo *et al.*, 2020; Guarnieri *et al.*, 2024; Mullen *et al.*,
105 2021). A central hallmark of this reprogramming leading to the accumulation of mitochondrial
106 reactive oxygen species (mROS) and consequent oxidative stress is the inhibition of
107 mitochondrial oxidative phosphorylation (OXPHOS) (Guarnieri *et al.*, 2024)**.** Elevated mROS
108 stabilises hypoxia-inducible factor 1-alpha (HIF-1α)**,** a key regulator that redirects cellular
109 metabolism toward glycolysis and the PPP, enhancing the synthesis and mobilisation of
110 nucleotides, lipids, and amino acids, which are necessary for viral replication (Guarnieri *et al.*,
111 2024; Mullen *et al.*, 2021). The virus also activates the mechanistic target of rapamycin
112 complex 1 (mTORC1) and integrated stress response (ISR) pathways, which in-turn promote
113 nutrient uptake, glycolysis, and innate immune signalling, while suppressing mitochondrial
114 biogenesis and cytosolic protein synthesis (Guarnieri *et al.*, 2024; Li *et al.*, 2021; Mullen *et al.*,

115 2021; Zambalde *et al*., 2022). In parallel, the virus disrupts cellular stress responses and
116 modulates key signalling pathways, such as the phosphoinositide 3-kinase/protein kinase B
117 (PI3K/AKT) and mitogen-activated protein kinase (MAPK) pathways, to promote cell survival
118 (Bojkova *et al.*, 2020; Li *et al.*, 2021; V'Kovski *et al.*, 2021). Despite these insights from early
119 variants, how such metabolic and signalling circuits have been refined or rewired in later
120 variants, particularly Delta and Omicron, remains poorly understood.
121
122 In this study, we focused on six epidemiologically and biologically representative SARS-CoV-2
123 lineages, which capture the principal stages of viral adaptation in replication dynamics,
124 immune evasion, and host metabolic engagement during the pandemic. Using an integrated
125 multi-omics approach in primary human nasal epithelial cells cultured at the air-liquid
126 interface, we compared their transcriptional, signalling, and metabolic responses at early and
127 late stages of infection to define lineage-specific strategies of host manipulation and their
128 implications for viral fitness and adaptation.
129
130 **Results**
131 Understanding how SARS-CoV-2 variants remodel host cell metabolism and signalling is
132 critical to deciphering their evolutionary adaptations in transmissibility and immune evasion.
133 To investigate these processes, primary nasal epithelial cells (NECs) from a pool of human
134 donors were cultured at the air-liquid interface and infected with three classes of SARS-CoV-
135 2 variants: early strains (IC19 (a lineage B.1 SARS-CoV-2 reference strain), the pre-Omicron:
136 Alpha, Beta), Delta, and Omicron subvariants (BA.1, and BA.5). NECs were derived from three
137 commercially available donor pools (MucilAir™, Epithelix), each comprising epithelial cells
138 from 10-14 independent human donors. This pooled design ensured physiological relevance

139 and helped minimise donor-specific variability across infection conditions. Viral replication
140 kinetics were measured over 72 hours. Transcriptomic analysis (RNA-seq) was conducted at
141 24 and 72 hpi, and phosphoproteomic and amino acid profiling were performed at 24 hpi to
142 characterise early post-translational and metabolic responses (Figure 1A).
143
144 **Omicron and Delta variants exhibit increased replication compared to pre-Omicron strains**
145 To compare the replication dynamics of SARS-CoV-2 variants, NECs were infected with the
146 variants at a multiplicity of infection (MOI) of 0.01, and viral genome copies in the culture
147 supernatants were quantified over time using *E* gene RT-qPCR (Figure 1B).
148 At 24 hpi, BA.1 exhibited the highest early replication, with significantly elevated viral genome
149 copies compared to the pre-Omicron reference strain IC19 ($p < 0.0001$), indicating an early
150 replication advantage. By 48 and 72 hpi, Delta showed the highest viral loads, significantly
151 exceeding IC19 at both time points ($p = 0.0014$ and 0.0029, respectively). BA.5 and Beta also
152 demonstrated increased replication relative to IC19, with significantly higher viral titres at 48
153 hpi ($p = 0.0165$ and 0.0173) and 72 hpi ($p = 0.0261$ and 0.0288). These findings demonstrate
154 group-specific replication dynamics, with Delta and Omicron subvariants exhibiting increased
155 replication efficiency in nasal epithelial cells compared to pre-Omicron strains.
156
157 **Delta triggers the most extensive transcriptional remodelling late in infection**
158 To characterise host transcriptional responses to SARS-CoV-2 variants, we performed RNA-
159 seq on NECs at 24 and 72 hpi (Figure 2A-C). Differentially expressed genes (DEGs) were
160 defined by a $\log_2$ fold change ≥ |1| and FDR ≤ 0.05 (Table S1). Key RNA-seq findings were
161 validated by qPCR for representative immune-signalling and metabolic genes (Supplementary
162 Figures S1–S2).

163 At 24 hpi, pre-Omicron variants (IC19, Alpha, and Beta) elicited the most substantial early
164 responses, with Alpha alone triggering over 3,800 DEGs (645 up-regulated, 3,162 down-
165 regulated). In contrast, Delta and the Omicron subvariants (BA.1 and BA.5) triggered markedly
166 fewer changes, suggesting attenuated or delayed early sensing (Figure 2B).
167 By 72 hpi, Delta drove the most extensive transcriptional reprogramming across all variants
168 (1,242 up-regulated, 4,432 down-regulated genes), while BA.1 and BA.5 induced intermediate
169 responses. Although some overlap in down-regulated genes was observed between Delta and
170 Omicron, the majority of DEGs remained variant-specific (Figure 2C).
171 Together, these data reveal distinct temporal transcriptional patterns across SARS-CoV-2
172 variants, with Delta driving the broadest late-stage reprogramming and highlighting the
173 evolving diversity of host–virus interactions.
174
175 **Reduced suppression of host interferon responses following infection with Omicron**
176 **subvariants**
177 We next examined how SARS-CoV-2 variants modulate innate antiviral signalling by
178 measuring interferon-stimulated gene (ISG) expression in primary nasal epithelial cells at 24
179 and 72 hpi (Figure 3A–D). ISGs represent core effectors of the type I interferon pathway and
180 provide a transcriptional readout of antiviral activation (Park and Iwasaki, 2020) (Figure 3A).
181 Cells treated with recombinant interferon alpha (IFN-α) were included as a reference to
182 establish a benchmark for ISG induction.
183 At 24 hpi, ISG induction remained low across all variant-infected relative to mock samples
184 (Figure 3B). Alpha and Beta showed the weakest early responses, whereas Delta and the
185 Omicron subvariants BA.1 and BA.5 triggered modest but detectable up-regulation. By 72 hpi,
186 ISG expression was broadly elevated, but with clear variant-specific differences (Figure 3C).

187 BA.1 and BA.5 induced the largest and most diverse ISG repertoires, similar in scale to those
188 induced by IFN-α, while Alpha and Beta exhibited more restricted activation. In contrast, Delta
189 consistently induced the fewest ISGs, even as infection advanced, pointing to sustained
190 suppression of interferon responses.
191 A heatmap of the top IFN-α-responsive ISGs (Figure 3D) further illustrates these differences.
192 BA.1 and BA.5 displayed relatively higher expression of canonical antiviral genes by 72 hpi
193 such as *CXCL10*, *ISG15*, *IFIT1*, and *OAS1*, key effectors of RNA sensing, translational arrest, and
194 immune recruitment (Schneider *et al.*, 2014; Schoggins, 2019; Schoggins *et al*., 2011),
195 compared with Delta. Compared with BA.1- and BA.5-infected cells, Delta-infected cells
196 showed fewer IFN-α–responsive genes and reduced expression levels, suggesting a weaker
197 activation of interferon signalling.
198
199 **Progressive tuning of host metabolism from early lineages to Delta and Omicron**
200 Previous reports have shown that early SARS-CoV-2 lineages, including IC19, Alpha, and Beta,
201 are associated with reduced mitochondrial activity and enhanced glycolytic flux, an
202 established viral strategy to redirect cellular resources toward biosynthesis (Codo *et al.*, 2020;
203 Guarnieri *et al.*, 2024; Mullen *et al.*, 2021). Cytosolic pathways such as glycolysis and the
204 pentose phosphate pathway (PPP) generate biosynthetic precursors, whereas mitochondrial
205 metabolism, including the tricarboxylic-acid (TCA) cycle, fatty-acid oxidation (FAO), and
206 oxidative phosphorylation (OXPHOS), supports ATP production, redox balance, and antiviral
207 signalling.
208 To investigate how infection with different SARS-CoV-2 variants correlates with metabolic
209 pathway changes in host cells, we performed gene set enrichment analysis (GSEA) of RNA-
210 seq data from NECs infected with the variants at 24 and 72 hpi, relative to uninfected controls

211 (Figure 4A-B). Normalised enrichment scores (NES) were used to quantify coordinated
212 transcriptional changes across curated metabolic pathways, providing a comparative measure
213 of pathway activation (positive NES) or suppression (negative NES) independent of gene-set
214 size and variance (Figure 4; full data is listed in Table S2). For interpretation, pathways with
215 an FDR < 0.05 were categorised by NES magnitude as follows: |NES| < 1.0, limited enrichment;
216 1.0 ≤ |NES| < 1.8, moderate enrichment; |NES| ≥ 1.8, strong enrichment.
217 At 24 hpi, metabolic responses were limited in magnitude (Figure 4A). Cells infected with most
218 variants showed near-neutral or mildly positive NES values in glycolysis and PPP, suggesting
219 modest early cytosolic engagement. FAO gene sets were consistently negative across
220 lineages, indicating an early block in β-oxidation. Mitochondrial carrier and import modules
221 were close to neutral, while OXPHOS complexes displayed small but generally positive
222 enrichment, apart from a modest negative enrichment in the Alpha/Beta Complex IV module.
223 Thus, early infection was associated with preserved or moderately enhanced respiratory-gene
224 expression rather than broad suppression.
225 By 72 hpi, clear lineage-specific profiles emerged (Figure 4B). Delta-infected cells exhibited
226 the highest and most coordinated positive NES across OXPHOS complexes I–V and several
227 mitochondrial modules, indicating strong respiratory activation accompanied by moderate
228 enrichment of glycolytic and lipid-metabolism pathways. Cells infected with the reference
229 strain IC19 retained moderate OXPHOS activation. Cells infected with pre-Omicron strains
230 displayed overall weaker enrichment and more variable mitochondrial responses. In contrast,
231 Omicron-infected cells showed near-neutral cytosolic NES, negative FAO and coenzyme Q
232 biosynthesis scores, and modest positive enrichment of mitochondrial-carrier and OXPHOS
233 modules, again with a negative Complex IV component. These findings suggest that Omicron

234 infection elicits a host response that maintains basal mitochondrial function while avoiding
235 extensive metabolic activation.
236 Grouped comparison (Figure 4B) summarises these three variant-specific trends. Cells
237 infected with early lineages (IC19, Alpha, Beta) show moderate OXPHOS enrichment at 24 hpi
238 that diminishes and becomes variable by 72 hpi. Delta-infected cells display the strongest and
239 most coordinated activation across respiratory and associated metabolic pathways. Omicron-
240 infected cells retain a selective, mitochondria-centred profile with positive overall OXPHOS
241 and minimal cytosolic activation.
242
243 **Delta activates stress kinases, while Omicron reprograms cytokine and survival signalling**
244 To characterise early host signalling responses, we next profiled phosphorylation events at 24
245 hpi in NECs infected with IC19, Delta, BA.1, and BA.5 using phospho-kinase arrays. These
246 variants were selected to represent the most distinct host-response patterns observed in our
247 dataset: IC19 as the ancestral reference, Delta as the lineage that showed the broadest
248 transcriptional and metabolic engagement in infected cells, and BA.1/BA.5 as Omicron
249 subvariants that, in our system, elicited comparatively restrained early responses but clearer
250 cytokine-linked signalling at later stages. Phosphorylation levels were normalised to mock
251 controls, and statistical significance was assessed using Welch's *t*-tests with Benjamini–
252 Hochberg correction (FDR < 0.05; Table S3).
253 Relative to mock, all infections were associated with phosphorylation changes in stress-,
254 growth-, and cytokine-associated proteins, but the magnitude and pattern differed markedly
255 between variants (Figure 5A–B). Compared with IC19-, Delta-infected cells displayed the
256 most extensive activation of cellular stress and translational pathways, with significant
257 increases in p53, PRAS40, and p70 kinase alongside higher phosphorylation of STAT3 and

258 STAT6. This profile suggests enhanced engagement of stress-responsive and translational
259 signalling pathways**.** Collectively, the pattern observed in Delta-infected cells is consistent
260 with a stress-associated and pro-survival phosphorylation signature dominated by the p53–
261 RSK–S6K and PRAS40 nodes.
262 By contrast, cells infected with Omicron subvariants exchibited phosphorylation patters
263 enriched in immune- and cytokine-linked pathways. BA.1-infected cells showed prominent
264 phosphorylation of p38 MAPK, PLC-γ1, RYK, and Src, alongside strong activation of JAK–STAT
265 components including STAT1, STAT2, and STAT5. Phosphorylation fold changes for STAT1
266 (11.7-fold) and STAT2 (4.0-fold) were the highest among all variants, consistent with strong
267 interferon- and cytokine-associated signalling. Cells infected with BA.5 showed a similar but
268 overall attenuated profile compared with BA.1, retaining phosphorylation of the p53, STAT3
269 (S727), and Src-family kinases.
270
271 **Contrasting host amino acid regulation by Delta and Omicron variants**
272 To complement the transcriptomic and phosphoproteomic analyses, intracellular amino acid
273 levels were quantified at 24 hpi in nasal epithelial cells infected with IC19, Delta, BA.1 or BA.5
274 and compared with mock-infected controls (Figure 6; Table S4). Total intracellular amino acid
275 abundance (Figure 6A) showed modest, non-significant reductions in IC19- and Delta-infected
276 cells ($q > 0.05$), despite an approximate 10% decrease in IC19 relative to mock. In contrast,
277 BA.1- and BA.5-infected cells exhibited significant reductions in total amino acid pools ($q <$
278 0.01 and $q < 0.05$, respectively). All amino acid measurements were expressed as nmol per
279 10^6 viable, counted cells, and viability at 24 hpi was comparable across conditions, indicating
280 that differences in abundance reflect infection-driven metabolic changes rather than
281 variation in cell number.

282 The variant–amino acid interaction network (Figure 6B) visualises these differences by linking
283 each variant to its most strongly altered amino acids. Edge width reflects the absolute $\log_2$
284 fold change, and colour indicates direction (red for increases, blue for decreases relative to
285 mock). BA.1 and BA.5 display numerous, broad negative edges, while IC19 and Delta show
286 fewer, thinner connections, consistent with a more limited metabolic impact.
287 Individual amino acid profiles (Figure 6C; Table S4) further resolved these patterns. In BA.1-
288 infected cells, intracellular amino acid levels showed the broadest and most significant
289 reductions, including all branched-chain and aromatic amino acids (leucine, phenylalanine,
290 tryptophan, isoleucine, valine), together with decreases in several other amino acids,
291 including threonine, serine, arginine and lysine. BA.5-infected cells exhibited a similar but less
292 pronounced profile, with significant decreases in many essential amino acids and moderate
293 increases in alanine and proline. Delta-infected cells displayed a mixed pattern, characterised
294 by significant increases in proline, alanine, glycine and glutamine, alongside reductions in
295 selected essential amino acids such as isoleucine and phenylalanine. IC19-infected cells
296 showed only small, variable changes, none of which reached significance after FDR correction.
297 To examine whether infection altered the internal balance of amino acids rather than total
298 abundance, amino acid levels were normalised to the total amino acid content within each
299 condition (Figure 6D; Table S4). The relative amino acid composition appeared consistent
300 across variants, suggesting that infection reduces overall amino acid availability without
301 disturbing the proportional balance within the intracellular pool.
302 Together, these data show that amino acid abundances in variant-infected cells differ from
303 those in mock-infected cells in a lineage-specific manner, with Delta-infected cells showing
304 comparatively higher levels of several biosynthetically relevant amino acids, whereas cells
305 infected with Omicron subvariants display broad amino acid depletion and limited

306 compensatory increases across pathways. Amino acids are central to energy production,
307 redox balance, protein synthesis, and immune signalling, and their intracellular abundance
308 provides a sensitive readout of metabolic stress and viral resource use (Thaker *et al.*, 2019).
309

310 **Discussion**

311 SARS-CoV-2 variants have evolved distinct capacities to replicate, modulate host immunity,
312 and influence disease severity. Although mechanisms of viral entry and antibody escape are
313 well characterised, far less is understood about how major lineages remodel host cellular
314 pathways once infection is established. To address this, we employed differentiated nasal
315 epithelial cells (NECs) grown at air-liquid interface, a physiologically relevant model that
316 recapitulates early epithelial infection in the absence of systemic immune influences. This
317 system enables direct examination of variant-specific host responses at the primary site of
318 replication, which may differ in magnitude and kinetics from those observed in bronchial or
319 immune-cell containing models. Through an integrated multi-omics approach, we uncovered
320 lineage-specific differences in the extent, timing, and coordination of transcriptional,
321 signalling, and metabolic responses.
322

323 Early lineages (IC19, Alpha, Beta) broadly down-regulated immune and metabolic transcripts
324 at 24 hpi, consistent with potent suppression of innate antiviral signalling. These results align
325 with previous studies showing that early SARS-CoV-2 isolates suppress mRNA synthesis and
326 translation through ORF6-, ORF8-, and ORF9b-mediated interference with STAT1/2 and
327 nuclear import (Laine *et al.*, 2022; Reuschl *et al.*, 2024; V'Kovski *et al.*, 2021; Yuen *et al.*, 2020).
328 By 72 hpi, infected nasal epithelial cells exhibited clear lineage-specific divergence. Cells
329 infected with Delta exhibited extensive transcriptional reprogramming, including activation

330 of stress-response, metabolic, and cytokine-related genes. In contrast, Omicron-infected cells
331 displayed fewer differentially expressed genes, nevertheless, showed selective enrichment of
332 interferon-stimulated and cytokine-responsive transcripts, consistent with a delayed yet
333 measurable antiviral response (Gori Savellini *et al.*, 2023; Reuschl *et al.*, 2024; Shi *et al.*, 2024).
334 Consistent with previously reported effective antagonism of RIG-I/MDA5–JAK–STAT signalling
335 (Laine *et al.*, 2022; Sievers *et al.*, 2024; Tandel *et al.*, 2022) IC19, Alpha, Beta, and Delta
336 displayed weak ISG induction at both 24 and 72 hpi. In contrast, Omicron elicited a broader
337 ISG response by 72 hpi, approaching that observed following exogenous IFN-α treatment,
338 suggesting only partial suppression of interferon-driven transcription (Reuschl *et al.*, 2024; Shi
339 *et al.*, 2024).
340 Phosphoproteomic profiling further distinguished variant phenotypes. Omicron infections
341 enhanced phosphorylation within JAK–STAT and MAPK modules (STAT1/2/5, p38, PLC-γ1,
342 Src), while Delta preferentially activated stress- and growth-associated kinases (p53, PRAS40,
343 RSK, p70 S6K), indicating engagement of PI3K–Akt–mTORC1 and the integrated stress
344 response (Bouhaddou *et al.*, 2020; Klann *et al.*, 2020; Li *et al.*, 2021). These patterns suggest
345 that Omicron can replicate despite ongoing cytokine signalling, whereas Delta infection
346 favours stress- and growth-linked pathways to sustain replication.
347 Our metabolic data reveal pronounced lineage-specific differences in host–virus
348 interaction. Consistent with previous reports (Codo *et al.*, 2020; Mullen *et al.*, 2021), cells
349 infected with pre-Omicron lineages suppressed fatty-acid oxidation and exhibited modest,
350 heterogenous mitochondrial changes, indicating partial mitochondrial adaptation rather than
351 broad inhibition. Conversely, Delta-infected cells displayed the strongest and most
352 coordinated activation spanning oxidative-phosphorylation complexes I–V and several
353 mitochondrial modules, accompanied by moderate enrichment of cytosolic pathways,

354 including the tricarboxylic-acid cycle and lipid metabolism. These transcriptional shifts
355 occurred despite broadly comparable viral loads across lineages at 24-72 hpi, suggesting that
356 replication level alone does not account for the observed metabolic divergence. Delta-
357 infected NECs retained or modestly increased one-carbon intermediates such as glycine,
358 glutamine, and alanine, consistent with preserved anabolic and redox capacity. Targeted
359 metabolomic analysis further revealed that total intracellular amino acid pools declined
360 across infections relative to mock, but the extent varied by lineage: Delta-infected cells
361 exhibited the smallest reduction, BA.5-infected cells an intermediate profile, and BA.1-
362 infected cells the most pronounced depletion, particularly of essential and branched-chain
363 amino acids such as leucine and valine. These findings indicate that Delta sustains a more
364 biosynthetically active state, whereas Omicron subvariants replicate under more
365 metabolically constrained conditions, suggesting a shift towards a low-anabolism infection
366 strategy. When amino acid levels were normalised to total intracellular content, the overall
367 proportional balance of amino acids in variant-infected cells was largely preserved, with only
368 a small deviation detected for BA.1 compared with mock. This pattern suggests that SARS-
369 CoV-2 lineages primarily modulate the metabolic tone of nasal epithelial cells by altering
370 amino acid availability, rather than by extensively reshaping the internal composition of the
371 amino acid pool.
372 Integration of transcriptomic, phosphoproteomic, and metabolic datasets, delineates three
373 distinct host-virus interaction strategies. Early lineages dampened transcription, interferon
374 signalling, and fatty-acid oxidation while maintaining only minimal mitochondrial activity.
375 Delta, by contrast, exhibited coordinated activation of respiratory, cytosolic, and stress
376 pathways, consistent with higher metabolic demand. Omicron retained efficient replication
377 while preserving mitochondrial respiration and tolerating interferon-linked signalling, yet

378 engaging anabolic metabolism only weakly. These lineage-specific programmes likely reflect
379 not only viral genetic differences but also the interplay between replication dynamics and
380 epithelial sensing thresholds in NECs. Overall, SARS-CoV-2 evolution appears to have
381 progressively re-tuned the balance between replication, metabolism, and immune
382 modulation. Later variants replicate effectively while imposing a smaller metabolic load and
383 causing less epithelial stress, yet remain capable of replication in the presence of active
384 cytokine and interferon responses. This restrained, energy-efficient infection profile mirrors
385 clinical observations that Omicron replication is largely confined to the upper airways and
386 associated with reduced epithelial injury and inflammation (Carabelli *et al.*, 2023; Gori
387 Savellini *et al.*, 2023; Laine *et al.*, 2022).
388 The use of pooled donor–derived NECs enhances physiological relevance but may mask inter-
389 individual variation in antiviral and metabolic responses. Future studies sampling additional
390 time points and integrating isotope-tracing could define metabolic flux through glycolysis and
391 the TCA cycle, while targeted perturbation of pathways such as PI3K–Akt–mTORC1, p53–RSK–
392 S6K, and p38 MAPK in ALI cultures could establish causal links between signalling nodes and
393 replication outcomes. Extending the approach to lower-airway or immune–epithelial co-
394 culture models would further connect cellular rewiring to tissue-level phenotypes and
395 transmissibility.
396 In summary, SARS-CoV-2 variants employ distinct reprogramming strategies in nasal
397 epithelium. Pre-Omicron strains strongly suppress antiviral and metabolic responses; Delta
398 drives extensive activation of stress and energy pathways; Omicron maintains mitochondrial
399 activity while limiting broader metabolic engagement. These contrasting strategies illustrate
400 how viral evolution has refined replication efficiency relative to metabolic demand and
401 immune modulation, providing mechanistic insight for host-targeted therapeutic approaches.

402 **Resource Availability**

403 **Lead Contact**

404 Further information and requests for resources and reagents should be directed to and will
405 be fulfilled by the Lead Contact, Dr Efstathios Giotis (e.giotis@essex.ac.uk).

406 **Materials availability**

407 No new unique reagents or biological materials were generated in this study. SARS-CoV-2
408 variant strains were obtained from existing publicly available virus collections, as indicated in
409 the Materials and Methods. All cell lines and virus isolates used are commercially or
410 institutionally available.

411 **Data and code availability**

412 The RNA sequencing data generated during this study have been deposited in the Gene
413 Expression Omnibus (GEO) under accession number GSE271378. The phosphoproteomic and
414 amino acid profiling datasets are available in the Supplemental information and can also be
415 shared upon request from the Lead Contact. This study generated analysis scripts for figure
416 production, available upon reasonable request from the Lead Contact. Scripts for data
417 visualisation (e.g., R scripts for heatmaps, Python for statistical plots) are available from the
418 Lead Contact upon reasonable request.

419

420 **Author contributions**

421 E.S.G. conceptualised the study, supervised the project, and contributed to methodology,
422 investigation, formal analysis, visualisation, and funding acquisition. R.A.S., J.B., T.A., N.B.,
423 D.L. and M.Mu. performed experimental work and contributed to methodology and
424 investigation. S.R.K. carried out bioinformatic analyses, formal analysis, data curation, and
425 visualisation. R.A.S. also contributed to data visualisation. M.Ra. conducted amino acid

426 profiling and provided resources and supervision. W.S.B. and C.R. contributed to project
427 supervision, resources, and funding acquisition. E.S.G., R.A.S., and S.R.K. wrote the original
428 draft, and all authors reviewed and edited the manuscript.
429

430 **Acknowledgements**

431 We are grateful to Juhi Kumar, Dorothee Reuss, Natalia Paulina Twardowska and Tom
432 Peacock for their technical assistance and helpful input during manuscript preparation. This
433 work was supported by the University of Essex COVID-19 Rapid and Agile Fund and the Faculty
434 of Science and Health Research Innovation and Support Fund. EG and DL are funded by an
435 MRC New Investigator Research Grant (MR/Z506242/1) and the Royal Society
436 (RGS\R2\242527). C.R. acknowledges support and funding from the Biotechnology and
437 Biological Sciences Research Council [Research grant numbers: BB/V006916/1,
438 BB/V006916/2] and from the Medical Research Council [Grant number: MR/W001462/1].
439 Wendy Barclay is supported in part by the NIHR Imperial Biomedical Research Centre (BRC).
440 Tukur Abdullahi is supported by the Nigerian Petroleum Technology Development Fund and
441 the University of Essex.

442 **Declaration of interests**

443 The authors declare no competing interests.

444 **Supplemental information**

445 **Supplementary Figures S1–S2**.

446 Contains validation of RNA-seq data by qPCR across selected immune signalling and
447 metabolic genes. Includes:

448 • **Supplementary Figure S1:** Correlation plot of RNA-seq vs qPCR fold-change values
449 for immune-signalling genes (*CXCL10, IFIT1, IFIT2, ISG15, OAS1, STAT1*).
450 • **Supplementary Figure S2:** Correlation plot of RNA-seq vs qPCR fold-change values
451 for metabolism-related genes (*HK2, GMPR, ENO2, MDH1B, ATP6V1B1*).

452 **Table S1.** Excel file containing DEG lists from RNA-sequencing analysis across SARS-CoV-2
453 variants, related to Figures 1 and 3.

454 **Table S2.** Normalised Enrichment Scores (NES) from fast Gene Set Enrichment Analysis
455 (fGSEA) of oxidative phosphorylation (OXPHOS), cytosolic and mitochondrial metabolic
456 pathways across SARS-CoV-2 variants and time points. NES, adjusted *p*-values (FDR), and
457 leading-edge gene counts are reported for each pathway.

458 **Table S3.** Excel file containing phospho-kinase array raw and processed data, related to
459 Figure 5.

460 **Table S4.** Excel file containing raw and normalised intracellular amino acid levels (nmol/10^6
461 cells), related to Figure 6.

462 **Table S5:** Primer sequences and RefSeq accession numbers used for qPCR validation.

463

464

465

466 **Figure Legends**

467 **Figure 1. Omicron and Delta variants exhibit enhanced replication compared to pre-**
468 **Omicron strains**

469 (**A**) **Schematic representation of the experimental setup.** Primary human nasal epithelial
470 cells were cultured at the air-liquid interface and infected with six SARS-CoV-2 variants: IC19
471 (reference strain), Alpha, Beta, Delta, Omicron BA.1, and Omicron BA.5. All infections were
472 performed at a multiplicity of infection (MOI) of 0.01. Parallel wells treated with recombinant
473 IFN-α served as a transcriptional benchmark. Cells were harvested at 24, 48, and 72 hpi for
474 downstream analyses, including phosphoproteomic profiling, amino acid (AA) profiling, and
475 RNA sequencing (RNA-seq). The timeline indicates the specific time points at which each
476 molecular analysis was conducted.

477 (**B**) **Growth kinetics of SARS-CoV-2 variants.** Viral replication over a 72-hour period was
478 quantified by RT-qPCR targeting the *E* gene. Viral RNA levels are expressed as *E* gene copies
479 per millilitre on a log10 scale. Measurements were taken at 0, 24, 48, and 72 hpi. Variants
480 Delta and BA.1 demonstrated significantly elevated viral loads compared to the reference
481 strain IC19 at multiple time points. Statistical significance was evaluated using one-way
482 ANOVA with Tukey's multiple comparisons test. Asterisks indicate significance levels: *$p <$
483 0.05, **$p < 0.01$, ***$p < 0.001$. Data are shown as mean ± standard deviation (SD) from three
484 independent experiments.

485

486 **Figure 2. Transcriptomic profiling of host responses to SARS-CoV-2 variant infection.**

487 (A) Number of significantly up-regulated (red) and down-regulated (blue) differentially
488 expressed genes (DEGs) at 24 and 72 hpi with indicated SARS-CoV-2 variants, based on RNA-
489 seq analysis (log2 fold-change ≥1; FDR <0.05).

490 (B) Venn diagrams showing shared and unique up-regulated DEGs among variants at 24 hpi
491 (top) and 72 hpi (bottom).
492 (C) Venn diagrams showing shared and unique down-regulated DEGs among variants at 24
493 hpi (top) and 72 hpi (bottom). Percentages represent overlap relative to the total DEGs per
494 variant.
495 **Figure 3. Late ISG induction by Omicron strains versus sustained attenuation by Delta**
496 (**A**) **Schematic of interferon signalling and ISG activation.**
497 (**B-C**) **Shared and unique ISG induction across variants at 24 (B) and 72 (C) hpi.** An UpSet plot
498 visualizes the number of significantly up-regulated ISGs (FDR < 0.05) per SARS-CoV-2 variant
499 and their overlaps. The bar chart at the top indicates the size of each intersection set, while
500 the connected dots below identify which variants contribute to each group. The colored
501 horizontal bars represent total ISG numbers detected per variant. The inset bar graphs show
502 the total number of significantly upregulated genes detected for each variant at the
503 corresponding time point, providing context for overall transcriptional activation.
504 (**D**) **Heatmaps showing log2 fold-change of top ISGs induced by IFNα treatment and during**
505 **infection at 24 and 72 hpi.** The leftmost panel shows the top ISGs up-regulated by IFNα
506 treatment alone, identifying baseline interferon responsiveness of the cells. The middle and
507 right panels show the expression of these ISGs in response to viral infection across all six SARS-
508 CoV-2 variants at 24 and 72 hpi, respectively. Color intensity reflects log2 fold-change, with
509 red indicating upregulation and blue indicating down-regulation or suppression.
510
511 **Figure 4. Normalised enrichment scores (NES) depict pathway-level transcriptional**
512 **changes across SARS-CoV-2 variants and time points.**
513 (**A**) Variant-specific NES profiles for cytosolic, mitochondrial, and oxidative phosphorylation

514 (OXPHOS) pathways at 24 and 72 hpi. Differential expression values (log_2 fold change) were
515 ranked and analysed with the fgsea R package using curated KEGG and literature-based
516 gene sets.
517 (**B**) Merged analysis comparing Pre-Omicron and Omicron lineages, showing composite NES
518 values summarizing transcriptional regulation across variants. Red indicates pathway
519 activation, blue indicates suppression. NES, normalised enrichment score.
520
521 **Figure 5. SARS-CoV-2 variants differentially regulate host signalling pathways through**
522 **phosphorylation events.**
523 (**A**) **Representative phospho-protein arrays** showing phosphorylation patterns in uninfected
524 mock controls and cells infected with IC19, Delta, Omicron BA.1, and Omicron BA.5 at 24
525 hpi. Key differentially phosphorylated proteins are highlighted.
526 (**B**) **Quantitative analysis of phosphorylation fold changes (variant-infected vs. mock)**
527 **across all array targets grouped by signalling pathway.** Dots represent mean values from at
528 least two independent experiments, with vertical error bars showing the standard error of
529 the mean (SEM). Colour coding denotes variant groups: IC19 (blue), Delta (orange), BA.1
530 (green), and BA.5 (red). Markers are ranked by biological pathway, with coloured
531 background shading corresponding to biological grouping. The vertical red dashed line
532 indicates the mock-infected baseline (fold change = 1).
533
534 **Figure 6. SARS-CoV-2 variants induce distinct amino acid reprogramming in nasal epithelial**
535 **cells.**
536 (**A**) **Bar plot showing total amino acid abundance** (nmol/10^6 cells) relative to mock-infected
537 controls at 24 hpi.

538 (**B**) **Variant–metabolite interaction network** showing amino acids (green nodes) connected
539 to each SARS-CoV-2 variant (grey nodes). Edges represent directionality of regulation
540 compared to mock: red edges indicate increased levels (upregulation), blue edges indicate
541 decreased levels (down-regulation), and black edges indicate no change.
542 (**C**) **Heatmap of log_2-transformed amino acid levels** (based on nmol/10^6 cells) for each
543 variant relative to mock-infected controls at 24 hpi. for each variant relative to mock-
544 infected controls at 24 hpi. Amino acids are annotated by metabolic pathway (left colour
545 bar) and biochemical role (right colour bar). Red shading indicates increased amino acid
546 abundance, and blue shading indicates decreased abundance**.**
547 **(D) Violin plots showing the % relative amino acid composition** after normalisation of each
548 amino acid to the total amino acid content within the same condition. This representation
549 highlights the internal proportional balance of amino acids rather than total abundance. The
550 black line indicates the median value for each distribution.
551
552
553 **MATERIALS AND METHODS**
554 **Cells and viruses**
555 Human nasal airway epithelial cells (NEC)s, maintained at the air–liquid interface
556 (MucilAir™, pooled from 14 donors, catalog no. EP02MP), were obtained in three batches
557 from Epithelix and cultured in MucilAir™ cell culture medium (Epithelix) at 37 °C with 5%
558 CO_2. SARS-CoV-2 variants were propagated and titrated as previously (Ogunjinmi *et al.*,
559 2024; Zhang *et al.*, 2022) in African green monkey kidney (VeroE6) cells expressing human
560 angiotensin-converting enzyme 2 (ACE2) and transmembrane protease serine 2 precursor
561 (TMPRSS2) (VAT), kindly provided by the MRC-University of Glasgow Centre for Virus

562 Research, Glasgow (Rihn *et al*., 2021). VAT cells were maintained in Dulbecco's Modified
563 Eagle Medium (DMEM) supplemented with 10% fetal calf serum (FCS), 1 mg/mL Geneticin
564 (Gibco), and 0.2 mg/mL Hygromycin B (Invitrogen). Viral stocks were generated and titrated
565 in VAT cells for the following SARS-CoV-2 variants: wild-type/D614G (hCoV-
566 19/England/IC19/2020, B.1.13, EPI_ISL_475572), Alpha (hCoV-19/England/205080610/2020,
567 B.1.1.7, EPI_ISL_723001), Delta (hCoV-19/England/SHEF-10E8F3B/2021, B.1.617.2,
568 EPI_ISL_1731019), Omicron BA.1 (hCoV-19/England/M21021166/2022, BA.1), and BA.5
569 (hCoV-19/England/NWLP_53/2022, BA.5).
570
571 **RNA-sequencing of nasal airway epithelial cells infected with SARS-CoV-2 variants**
572 Before infection, NEC cultures were washed with serum-free medium to remove mucus and
573 debris. Cells were then infected with 200 µL of virus-containing serum-free DMEM (MOI: 0.01)
574 and incubated at 37 °C for 1 hour. Following incubation, the inoculum was removed, and the
575 cells were washed twice. Time points were collected by adding 200 µL of serum-free DMEM,
576 incubating at 37 °C for 10 minutes, and then removing the medium for titration. Cells were
577 harvested at 24 and 72 hours for RNA isolation using the RNeasy Mini Plus kit (Qiagen), and
578 approximately 1 µg of RNA was used for sequencing library preparation.
579 mRNA libraries were prepared using poly-A enrichment and sequenced by Novogene. The
580 sequencing data (FASTQ raw files) were imported into Partek Flow (version 10.0, build
581 10.0.23.0531; Partek Inc.) for quality control and processing. Paired-end reads were trimmed
582 based on a Phred quality score threshold of >20 and aligned to the human genome (hg38)
583 using the STAR-2.7.8a aligner. Gene expression was quantified using the Ensembl Transcripts
584 release 104 v2 transcript model, and data were normalised using the counts per million (CPM)
585 method. Differential gene expression analysis was conducted using the DESeq2 package, with

586 genes considered differentially expressed if they met the criteria of FDR ≤ 0.05 and a log2 fold
587 change ≥ |1|. All RNA-seq data have been deposited in the Gene Expression Omnibus (GEO)
588 under accession number GSE271378.
589
590 **Pathway enrichment and transcriptomic profiling**
591 Normalised enrichment scores (NES) generated from the fGSEA analysis were visualised using
592 dot plots in R (v4.3) with the *ggplot2* (v3.4.4), *dplyr*, *tidyr*, *stringr*, and *readxl* packages. Each
593 dot represented a metabolic pathway under a specific condition, where the horizontal axis
594 denoted NES magnitude and the vertical axis listed the curated gene sets (cytosolic,
595 mitochondrial, and oxidative phosphorylation). Dot colour indicated the direction of
596 regulation (red, up-regulated; blue, down-regulated), and dot size was proportional to the
597 absolute NES value. Vertical reference lines at NES = 0 were included to indicate neutral
598 enrichment.
599 To aid visual interpretation, NES magnitudes were categorised as limited (|NES| < 1.0),
600 moderate (1.0 ≤ |NES| < 1.8), or strong (|NES| ≥ 1.8) enrichment. Only pathways meeting the
601 inclusion criteria defined in the differential expression analysis were displayed. While the dot
602 plots provide a comparative overview of pathway-level regulation, they represent aggregate
603 enrichment statistics rather than individual gene contributions. Adjusted *p*-values and false
604 discovery rates (FDR) computed during fGSEA were not visualised in the figure but are
605 reported in Supplementary Table S2. Pathway sizes (number of genes per set) and inter-gene
606 variance were not displayed to maintain visual clarity; therefore, pathways of different gene-
607 set sizes appear equally weighted. Similarly, replicate-level variability and confidence
608 intervals for NES values were not plotted, as the scores reflect ranked enrichment rather than
609 absolute expression magnitude. Relationships between overlapping pathways were not

610 visualised but were accounted for during pathway curation. Together, these dot plots
611 summarise the direction and magnitude of metabolic pathway enrichment across SARS-CoV-
612 2 variants and time points while maintaining a uniform visual scale for comparative
613 assessment.
614
615 **Quantification of viral and host gene expression by RT-qPCR**
616 Virus genome quantification was carried out using *E* gene RT-qPCR, following a previously
617 described method (Zhou *et al.*, 2022). Viral RNA was extracted from swab supernatant
618 samples using the QIAsymphony DSP Virus/Pathogen Mini Kit on the QIAsymphony
619 instrument (Qiagen). RT-qPCR was performed with the AgPath RT-PCR kit (Life Technologies)
620 on a QuantStudio 7 Flex Real-Time PCR System, using primers specific to the SARS-CoV-2 *E*
621 gene (Corman *et al.*, 2020). For absolute quantification of *E* gene RNA copies, a standard curve
622 was generated from serial dilutions of viral RNA with a known copy number. The *E* gene copies
623 per ml of the original virus supernatant were then determined based on this standard curve.
624
625 **Validation of RNA-sequencing data by quantitative RT-PCR**
626 To validate differential gene expression observed in RNA-seq, we performed quantitative
627 RT-PCR (qPCR) using independently designed primers as before (Giotis et al., 2019;
628 Ogunjinmi *et al.*, 2024; Zhang *et al.*, 2022). Genes were selected based on their
629 transcriptional regulation across SARS-CoV-2 variants and their relevance to innate immune
630 signalling (e.g., *CXCL10, IFIT1, IFIT2*, *ISG15*, *OAS1, STAT1*) or metabolic pathways (e.g., *HK2*,
631 *GMPR, MDH1B*, *ENO2, ATP6V1B1*). Total RNA was extracted from nasal epithelial cell
632 cultures using TRIzol™ Reagent (Fisher Scientific) according to the manufacturer's protocol.
633 qPCR was carried out on a CFX96 Real-Time PCR System (Bio-Rad) using PowerUp™ SYBR

634 Green Master Mix (Fisher Scientific). All reactions were run in triplicate to ensure
635 reproducibility. Primer sequences, designed based on NCBI RefSeq transcripts, are listed in
636 Table S5.
637
638 **Phospho-kinase array and signalling analysis**
639 Phosphorylation profiling was carried out using the Proteome Profiler Human Phospho-Kinase
640 Array Kit (ARY003B, R&D Systems), which detects phosphorylation at 43 kinase sites across
641 multiple host signalling pathways. Arrays were performed on lysates collected at 24 hpi from
642 the same nasal epithelial cell cultures used for transcriptomic and amino acid profiling,
643 ensuring matched experimental conditions across assays. Following protein extraction, total
644 protein was quantified using the Pierce BCA Protein Assay Kit (Thermo Scientific), and equal
645 amounts of lysate were incubated with array membranes overnight at 4 °C, according to the
646 manufacturer's instructions. Chemiluminescent signals were developed using SuperSignal
647 West Femto substrate (Thermo Scientific) and imaged with the Invitrogen iBright FL1500
648 system. Spot intensities were quantified in ImageJ (v1.53), corrected for background, and
649 normalised to internal reference spots. Fold changes were calculated relative to mock-
650 infected controls. Each condition was assessed in at least two independent experiments. Data
651 visualisation was performed in Python (v3.10) using seaborn and matplotlib. Phosphorylation
652 sites were grouped by pathway (e.g., PI3K-Akt, MAPK, JAK-STAT) based on KEGG and
653 Reactome annotations (Figure 5). Dot plots represent mean fold changes ± SEM, with the
654 mock baseline shown as a red dashed line.
655
656
657

658 **Quantitative amino acid profiling and network-based visualisation of metabolic disruption**

659 Amino acid analysis was performed using hydrophilic interaction chromatography-tandem
660 mass spectrometry (HILIC-MS/MS), similar as previously described (Jeffares *et al.*, 2015;
661 Mulleder *et al.*, 2017; Rallis *et al.*, 2021). We used four biological replicates per condition,
662 each processed in duplicate (two technical replicates), to ensure robustness and
663 reproducibility of quantification. One million cells were harvested per condition (mock and
664 viral infections). For extraction, cells were pelleted (3000g, 3 min), washed briefly, and
665 resuspended in 200 µL of 80% ethanol preheated to 80 °C. The suspension was vortexed and
666 incubated at 80 °C for 2 minutes, repeated once, then centrifuged at maximum speed for 2
667 minutes to clear cell debris and stored at 80 °C until further usage. For the exact amino acid
668 quantification, we included cell free $^{15}N^{13}C$ labelled amino acids as internal standard (CNLM-
669 6696-PK, Cambridge Isotope Laboratories). Besides, a calibration curve was generated using
670 serial dilutions of standards. The amino acid measurements were performed by using a
671 flowrate of 0.6 ml/min for 12 min. All proteinogenic amino acids amino expect cysteine were
672 measured.

673 Final amino acid concentrations were expressed as nanomoles (nmol) per 10^6 cells to
674 normalise for input cell number across conditions (Table S4). To visualise SARS-CoV-2 variant-
675 specific amino acid expression changes, a bipartite node network was constructed using
676 Python (pandas, numpy, networkx, matplotlib). Amino acid $\log_2$ fold changes relative to mock
677 at 24 hpi (Table S4) were used to identify the top five most dysregulated amino acids per
678 variant (ranked by absolute $\log_2$ fold change). These variant–amino acid pairs formed the
679 network edges. Edge thickness reflected the magnitude of the change, while colour indicated
680 direction: red (increased abundance), blue (decreased abundance), and black (no substantial
681 change). Amino acid nodes were sized by total connectivity and coloured according to their

682 dominant direction of change across variants**.** The layout was manually optimised for clarity.
683 This network allowed integrated visualisation of shared and distinct metabolic disruptions
684 across variants, complementing the quantitative $\log_2$ fold-change data presented in
685 heatmaps.
686
687 **Statistical analysis**
688 All data were analysed using GraphPad Prism software (v9) and Python (v3.10). Results are
689 presented as mean ± SEM. Statistical significance was defined as $p < 0.05$, with levels of
690 significance indicated as follows: $p < 0.05$ (**), $p < 0.01$ (**), and $p < 0.001$ (***).
691 To assess differences in viral replication between SARS-CoV-2 variants at each time point
692 relative to the reference strain IC19, a one-way ANOVA was performed at 0, 24, 48, and 72
693 hpi. If statistical significance ($p < 0.05$) was observed, Tukey's Honest Significant Difference
694 (HSD) test was conducted for post-hoc pairwise comparisons to determine specific
695 differences between IC19 and each variant. Adjusted p-values from Tukey's HSD test were
696 used to control for multiple comparisons, ensuring robust identification of significant
697 replication differences. Variants exhibiting p-values below the 0.05 threshold were
698 considered to have significant replication advantages or disadvantages relative to IC19.
699 Results were annotated on viral growth curves to highlight meaningful differences across the
700 infection timeline.
701 Phospho-array data were log-transformed data and analysed using Welch's t-tests, followed
702 by Benjamini-Hochberg correction for multiple comparisons (Table S4). Amino acid
703 concentrations (nmol per 10^6 cells) were measured in four biological replicates per condition,
704 each processed in duplicate. Technical replicates were averaged per biological replicate
705 before statistical analysis. For each amino acid, mean values were used to calculate the fold

706 change relative to mock and the corresponding $\log_2$ fold change ($\log_2FC = \log_2$[variant/mock]).
707 Statistical testing was performed using Welch's two-sample t-tests (unequal variances)
708 applied to each amino acid for: (i) comparisons of each SARS-CoV-2 variant against mock, and
709 (ii) all pairwise comparisons between conditions (mock, IC19, Delta, BA.1, BA.5). Multiple
710 testing within each comparison was corrected using the Benjamini–Hochberg false discovery
711 rate (FDR) procedure (threshold $q < 0.05$). Table S4 reports, for each amino acid and
712 comparison, the raw p value, the FDR-adjusted q value, a Yes/No column indicating
713 significance at $q < 0.05$, and p-value significance symbols (* $p < 0.05$; ** $p < 0.01$; *** $p <$
714 0.001; **** $p < 0.0001$; ns for non-significant). Log_2FC values are provided as effect sizes.
715 To assess whether infection altered amino acid composition independently of total
716 abundance, amino acid levels were normalised to the total amino acid content within each
717 condition. The resulting relative proportions were compared across variants using the
718 Friedman test with Dunn's multiple-comparison correction (GraphPad Prism v9). Total amino
719 acid abundance per condition was calculated by summing per–amino acid means, with
720 percent change expressed relative to Mock.
721
722 **Data visualisation**
723 To illustrate shifts in amino acid levels across SARS-CoV-2 variants, heatmaps and summary
724 tables were used to facilitate interpretation and guide RNA-seq pathway analysis. For
725 phosphoproteomic analyses, heatmaps were generated using Python's matplotlib and
726 seaborn libraries. Heatmap of amino acid fold changes were generated using
727 the pheatmap package in R (v4.3), clustering both rows and columns to reveal variant-specific
728 metabolite patterns. Venn diagrams were created with InteractiVenn (Heberle *et al.*, 2015) to
729 analyse shared and unique features across different conditions.

References

Allen, C.N.S., Arjona, S.P., Santerre, M., and Sawaya, B.E. (2022). Hallmarks of Metabolic Reprogramming and Their Role in Viral Pathogenesis. Viruses *14*. 10.3390/v14030602.

Bojkova, D., Klann, K., Koch, B., Widera, M., Krause, D., Ciesek, S., Cinatl, J., and Munch, C. (2020). Proteomics of SARS-CoV-2-infected host cells reveals therapy targets. Nature *583*, 469-472. 10.1038/s41586-020-2332-7.

Bouhaddou, M., Memon, D., Meyer, B., White, K.M., Rezelj, V.V., Correa Marrero, M., Polacco, B.J., Melnyk, J.E., Ulferts, S., Kaake, R.M., et al. (2020). The Global Phosphorylation Landscape of SARS-CoV-2 Infection. Cell *182*, 685-712 e619. 10.1016/j.cell.2020.06.034.

Carabelli, A.M., Peacock, T.P., Thorne, L.G., Harvey, W.T., Hughes, J., Consortium, C.-G.U., Peacock, S.J., Barclay, W.S., de Silva, T.I., Towers, G.J., and Robertson, D.L. (2023). SARS-CoV-2 variant biology: immune escape, transmission and fitness. Nat Rev Microbiol *21*, 162-177. 10.1038/s41579-022-00841-7.

Chan, E.Y., Sutton, J.N., Jacobs, J.M., Bondarenko, A., Smith, R.D., and Katze, M.G. (2009). Dynamic host energetics and cytoskeletal proteomes in human immunodeficiency virus type 1-infected human primary CD4 cells: analysis by multiplexed label-free mass spectrometry. J Virol *83*, 9283-9295. 10.1128/JVI.00814-09.

Codo, A.C., Davanzo, G.G., Monteiro, L.B., de Souza, G.F., Muraro, S.P., Virgilio-da-Silva, J.V., Prodonoff, J.S., Carregari, V.C., de Biagi Junior, C.A.O., Crunfli, F., et al. (2020). Elevated Glucose Levels Favor SARS-CoV-2 Infection and Monocyte Response through a HIF-1alpha/Glycolysis-Dependent Axis. Cell Metab *32*, 437-446 e435. 10.1016/j.cmet.2020.07.007.

Corman, V.M., Landt, O., Kaiser, M., Molenkamp, R., Meijer, A., Chu, D.K., Bleicker, T., Brunink, S., Schneider, J., Schmidt, M.L., et al. (2020). Detection of 2019 novel coronavirus (2019-nCoV) by real-time RT-PCR. Euro Surveill *25*. 10.2807/1560-7917.ES.2020.25.3.2000045.

Desmyter, J., Melnick, J.L., and Rawls, W.E. (1968). Defectiveness of interferon production and of rubella virus interference in a line of African green monkey kidney cells (Vero). J Virol *2*, 955-961. 10.1128/JVI.2.10.955-961.1968.

Giotis, E.S., Carnell, G., Young, E.F., Ghanny, S., Soteropoulos, P., Wang, L.F., Barclay, W.S., Skinner, M.A., and Temperton, N. (2019). Entry of the bat influenza H17N10 virus into mammalian cells is enabled by the MHC class II HLA-DR receptor. Nat Microbiol *4*, 2035-2038. 10.1038/s41564-019-0517-3.

Giotis, E.S., Cil, E., and Brooke, G.N. (2022). Use of Antiandrogens as Therapeutic Agents in COVID-19 Patients. Viruses *14*. 10.3390/v14122728.

Gori Savellini, G., Anichini, G., and Cusi, M.G. (2023). SARS-CoV-2 omicron sub-lineages differentially modulate interferon response in human lung epithelial cells. Virus Res *332*, 199134. 10.1016/j.virusres.2023.199134.

Guarnieri, J.W., Haltom, J.A., Albrecht, Y.E.S., Lie, T., Olali, A.Z., Widjaja, G.A., Ranshing, S.S., Angelin, A., Murdock, D., and Wallace, D.C. (2024). SARS-CoV-2 mitochondrial metabolic and epigenomic reprogramming in COVID-19. Pharmacol Res *204*, 107170. 10.1016/j.phrs.2024.107170.

Harvey, W.T., Carabelli, A.M., Jackson, B., Gupta, R.K., Thomson, E.C., Harrison, E.M., Ludden, C., Reeve, R., Rambaut, A., Consortium, C.-G.U., et al. (2021). SARS-CoV-2 variants, spike mutations and immune escape. Nat Rev Microbiol *19*, 409-424. 10.1038/s41579-021-00573-0.

774 Heberle, H., Meirelles, G.V., da Silva, F.R., Telles, G.P., and Minghim, R. (2015). InteractiVenn:
775 a web-based tool for the analysis of sets through Venn diagrams. BMC Bioinformatics *16*, 169.
776 10.1186/s12859-015-0611-3.
777 Jeffares, D.C., Rallis, C., Rieux, A., Speed, D., Prevorovsky, M., Mourier, T., Marsellach, F.X.,
778 Iqbal, Z., Lau, W., Cheng, T.M., et al. (2015). The genomic and phenotypic diversity of
779 Schizosaccharomyces pombe. Nat Genet *47*, 235-241. 10.1038/ng.3215.
780 Klann, K., Bojkova, D., Tascher, G., Ciesek, S., Munch, C., and Cinatl, J. (2020). Growth Factor
781 Receptor Signaling Inhibition Prevents SARS-CoV-2 Replication. Mol Cell *80*, 164-174 e164.
782 10.1016/j.molcel.2020.08.006.
783 Laine, L., Skon, M., Vaisanen, E., Julkunen, I., and Osterlund, P. (2022). SARS-CoV-2 variants
784 Alpha, Beta, Delta and Omicron show a slower host cell interferon response compared to an
785 early pandemic variant. Front Immunol *13*, 1016108. 10.3389/fimmu.2022.1016108.
786 Leach, D.A., Mohr, A., Giotis, E.S., Cil, E., Isac, A.M., Yates, L.L., Barclay, W.S., Zwacka, R.M.,
787 Bevan, C.L., and Brooke, G.N. (2021). The antiandrogen enzalutamide downregulates
788 TMPRSS2 and reduces cellular entry of SARS-CoV-2 in human lung cells. Nat Commun *12*,
789 4068. 10.1038/s41467-021-24342-y.
790 Li, F., Li, J., Wang, P.H., Yang, N., Huang, J., Ou, J., Xu, T., Zhao, X., Liu, T., Huang, X., et al. (2021).
791 SARS-CoV-2 spike promotes inflammation and apoptosis through autophagy by ROS-
792 suppressed PI3K/AKT/mTOR signaling. Biochim Biophys Acta Mol Basis Dis *1867*, 166260.
793 10.1016/j.bbadis.2021.166260.
794 Liu, P.J., Harris, J.M., Marchi, E., D'Arienzo, V., Michler, T., Wing, P.A.C., Magri, A., Ortega-Prieto,
795 A.M., van de Klundert, M., Wettengel, J., et al. (2020). Hypoxic gene expression in chronic
796 hepatitis B virus infected patients is not observed in state-of-the-art in vitro and mouse
797 infection models. Sci Rep *10*, 14101. 10.1038/s41598-020-70865-7.
798 Liu, Y., and Rocklov, J. (2021). The reproductive number of the Delta variant of SARS-CoV-2 is
799 far higher compared to the ancestral SARS-CoV-2 virus. J Travel Med *28*. 10.1093/jtm/taab124.
800 Long, J.S., Giotis, E.S., Moncorge, O., Frise, R., Mistry, B., James, J., Morisson, M., Iqbal, M.,
801 Vignal, A., Skinner, M.A., and Barclay, W.S. (2016). Species difference in ANP32A underlies
802 influenza A virus polymerase host restriction. Nature *529*, 101-104. 10.1038/nature16474.
803 Mulleder, M., Bluemlein, K., and Ralser, M. (2017). A High-Throughput Method for the
804 Quantitative Determination of Free Amino Acids in Saccharomyces cerevisiae by Hydrophilic
805 Interaction Chromatography-Tandem Mass Spectrometry. Cold Spring Harb Protoc *2017*, pdb
806 prot089094. 10.1101/pdb.prot089094.
807 Mullen, P.J., Garcia, G., Jr., Purkayastha, A., Matulionis, N., Schmid, E.W., Momcilovic, M., Sen,
808 C., Langerman, J., Ramaiah, A., Shackelford, D.B., et al. (2021). SARS-CoV-2 infection rewires
809 host cell metabolism and is potentially susceptible to mTORC1 inhibition. Nat Commun *12*,
810 1876. 10.1038/s41467-021-22166-4.
811 Ogunjinmi, O.D., Abdullahi, T., Somji, R.A., Bevan, C.L., Barclay, W.S., Temperton, N., Brooke,
812 G.N., and Giotis, E.S. (2024). The antiviral potential of the antiandrogen enzalutamide and the
813 viral-androgen signaling interplay in seasonal coronaviruses. J Med Virol *96*, e29540.
814 10.1002/jmv.29540.
815 Park, A., and Iwasaki, A. (2020). Type I and Type III Interferons - Induction, Signaling, Evasion,
816 and Application to Combat COVID-19. Cell Host Microbe *27*, 870-878.
817 10.1016/j.chom.2020.05.008.
818 Polcicova, K., Badurova, L., and Tomaskova, J. (2020). Metabolic reprogramming as a feast for
819 virus replication. Acta Virol *64*, 201-215. 10.4149/av_2020_210.

Rajah, M.M., Hubert, M., Bishop, E., Saunders, N., Robinot, R., Grzelak, L., Planas, D., Dufloo, J., Gellenoncourt, S., Bongers, A., et al. (2021). SARS-CoV-2 Alpha, Beta, and Delta variants display enhanced Spike-mediated syncytia formation. EMBO J *40*, e108944. 10.15252/embj.2021108944.

Rallis, C., Mulleder, M., Smith, G., Au, Y.Z., Ralser, M., and Bahler, J. (2021). Amino Acids Whose Intracellular Levels Change Most During Aging Alter Chronological Life Span of Fission Yeast. J Gerontol A Biol Sci Med Sci *76*, 205-210. 10.1093/gerona/glaa246.

Reuschl, A.K., Thorne, L.G., Whelan, M.V.X., Ragazzini, R., Furnon, W., Cowton, V.M., De Lorenzo, G., Mesner, D., Turner, J.L.E., Dowgier, G., et al. (2024). Evolution of enhanced innate immune suppression by SARS-CoV-2 Omicron subvariants. Nat Microbiol *9*, 451-463. 10.1038/s41564-023-01588-4.

Rihn, S.J., Merits, A., Bakshi, S., Turnbull, M.L., Wickenhagen, A., Alexander, A.J.T., Baillie, C., Brennan, B., Brown, F., Brunker, K., et al. (2021). A plasmid DNA-launched SARS-CoV-2 reverse genetics system and coronavirus toolkit for COVID-19 research. PLoS Biol *19*, e3001091. 10.1371/journal.pbio.3001091.

Ritter, J.B., Wahl, A.S., Freund, S., Genzel, Y., and Reichl, U. (2010). Metabolic effects of influenza virus infection in cultured animal cells: Intra- and extracellular metabolite profiling. BMC Syst Biol *4*, 61. 10.1186/1752-0509-4-61.

Schneider, W.M., Chevillotte, M.D., and Rice, C.M. (2014). Interferon-stimulated genes: a complex web of host defenses. Annu Rev Immunol *32*, 513-545. 10.1146/annurev-immunol-032713-120231.

Schoggins, J.W. (2019). Interferon-Stimulated Genes: What Do They All Do? Annu Rev Virol *6*, 567-584. 10.1146/annurev-virology-092818-015756.

Schoggins, J.W., Wilson, S.J., Panis, M., Murphy, M.Y., Jones, C.T., Bieniasz, P., and Rice, C.M. (2011). A diverse range of gene products are effectors of the type I interferon antiviral response. Nature *472*, 481-485. 10.1038/nature09907.

Shi, G., Li, T., Lai, K.K., Johnson, R.F., Yewdell, J.W., and Compton, A.A. (2024). Omicron Spike confers enhanced infectivity and interferon resistance to SARS-CoV-2 in human nasal tissue. Nat Commun *15*, 889. 10.1038/s41467-024-45075-8.

Sievers, B.L., Cheng, M.T.K., Csiba, K., Meng, B., and Gupta, R.K. (2024). SARS-CoV-2 and innate immunity: the good, the bad, and the "goldilocks". Cell Mol Immunol *21*, 171-183. 10.1038/s41423-023-01104-y.

Singh, M., Bansal, V., and Feschotte, C. (2020). A Single-Cell RNA Expression Map of Human Coronavirus Entry Factors. Cell Rep *32*, 108175. 10.1016/j.celrep.2020.108175.

Sposito, B., Broggi, A., Pandolfi, L., Crotta, S., Clementi, N., Ferrarese, R., Sisti, S., Criscuolo, E., Spreafico, R., Long, J.M., et al. (2021). The interferon landscape along the respiratory tract impacts the severity of COVID-19. Cell *184*, 4953-4968 e4916. 10.1016/j.cell.2021.08.016.

Sungnak, W., Huang, N., Becavin, C., Berg, M., Queen, R., Litvinukova, M., Talavera-Lopez, C., Maatz, H., Reichart, D., Sampaziotis, F., et al. (2020). SARS-CoV-2 entry factors are highly expressed in nasal epithelial cells together with innate immune genes. Nat Med *26*, 681-687. 10.1038/s41591-020-0868-6.

Tandel, D., Sah, V., Singh, N.K., Potharaju, P.S., Gupta, D., Shrivastava, S., Sowpati, D.T., and Harshan, K.H. (2022). SARS-CoV-2 Variant Delta Potently Suppresses Innate Immune Response and Evades Interferon-Activated Antiviral Responses in Human Colon Epithelial Cells. Microbiol Spectr *10*, e0160422. 10.1128/spectrum.01604-22.

Thaker, S.K., Ch'ng, J., and Christofk, H.R. (2019). Viral hijacking of cellular metabolism. BMC Biol *17*, 59. 10.1186/s12915-019-0678-9.

867 V'Kovski, P., Kratzel, A., Steiner, S., Stalder, H., and Thiel, V. (2021). Coronavirus biology and
868 replication: implications for SARS-CoV-2. Nat Rev Microbiol *19*, 155-170. 10.1038/s41579-020-
869 00468-6.
870 Yuen, C.K., Lam, J.Y., Wong, W.M., Mak, L.F., Wang, X., Chu, H., Cai, J.P., Jin, D.Y., To, K.K., Chan,
871 J.F., et al. (2020). SARS-CoV-2 nsp13, nsp14, nsp15 and orf6 function as potent interferon
872 antagonists. Emerg Microbes Infect *9*, 1418-1428. 10.1080/22221751.2020.1780953.
873 Zambalde, E.P., Dias, T.L., Maktura, G.C., Amorim, M.R., Brenha, B., Santos, L.N., Buscaratti, L.,
874 Elston, J.G.A., Mancini, M.C.S., Pavan, I.C.B., et al. (2022). Increased mTOR Signaling and
875 Impaired Autophagic Flux Are Hallmarks of SARS-CoV-2 Infection. Curr Issues Mol Biol *45*, 327-
876 336. 10.3390/cimb45010023.
877 Zhang, Z., Penn, R., Barclay, W.S., and Giotis, E.S. (2022). Naive Human Macrophages Are
878 Refractory to SARS-CoV-2 Infection and Exhibit a Modest Inflammatory Response Early in
879 Infection. Viruses *14*. 10.3390/v14020441.
880 Zhou, J., Peacock, T.P., Brown, J.C., Goldhill, D.H., Elrefaey, A.M.E., Penrice-Randal, R., Cowton,
881 V.M., De Lorenzo, G., Furnon, W., Harvey, W.T., et al. (2022). Mutations that adapt SARS-CoV-
882 2 to mink or ferret do not increase fitness in the human airway. Cell Rep *38*, 110344.
883 10.1016/j.celrep.2022.110344.

884

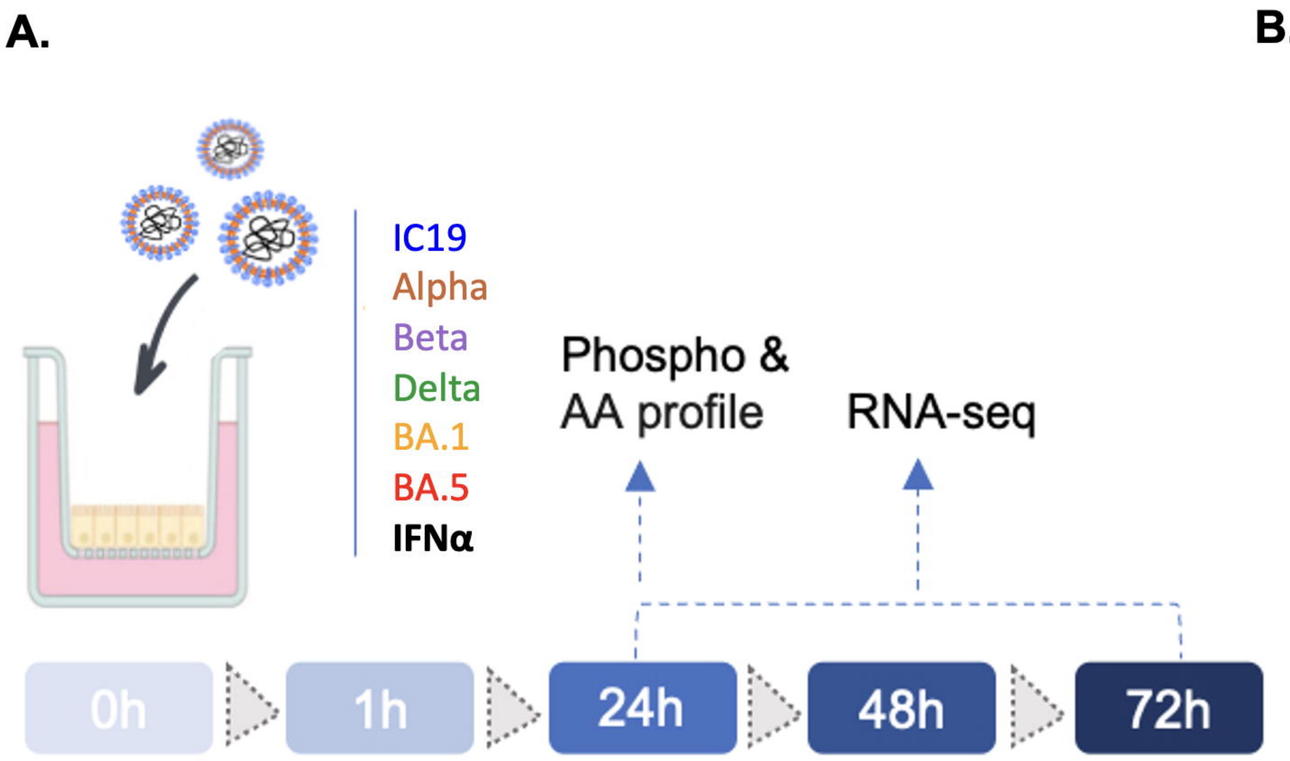
A.
IC19
Alpha
Beta
Delta
BA.1
BA.5
IFNα
Phospho &
AA profile
RNA-seq
0h
1h
24h
48h
72h

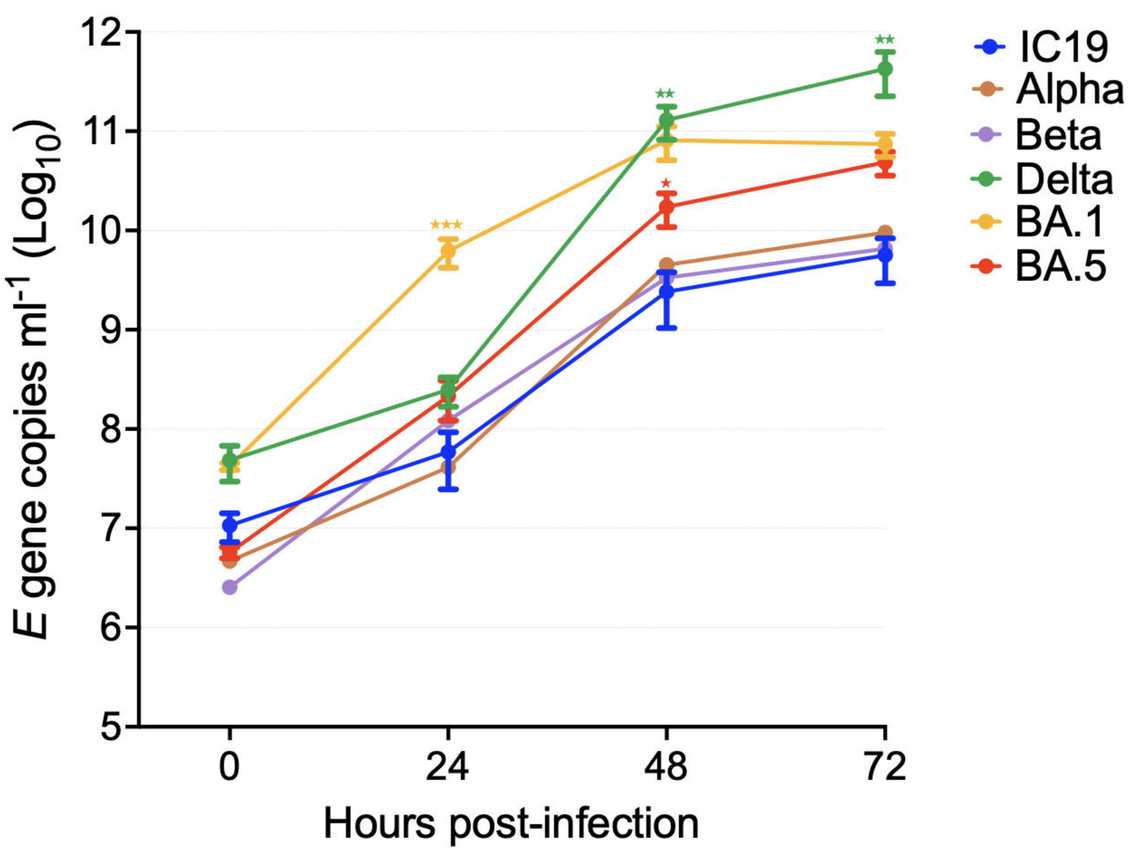
B.
E gene copies ml-1 (Log10)
12
11
10
9
8
7
6
5
0
24
48
72
Hours post-infection
IC19
Alpha
Beta
Delta
BA.1
BA.5

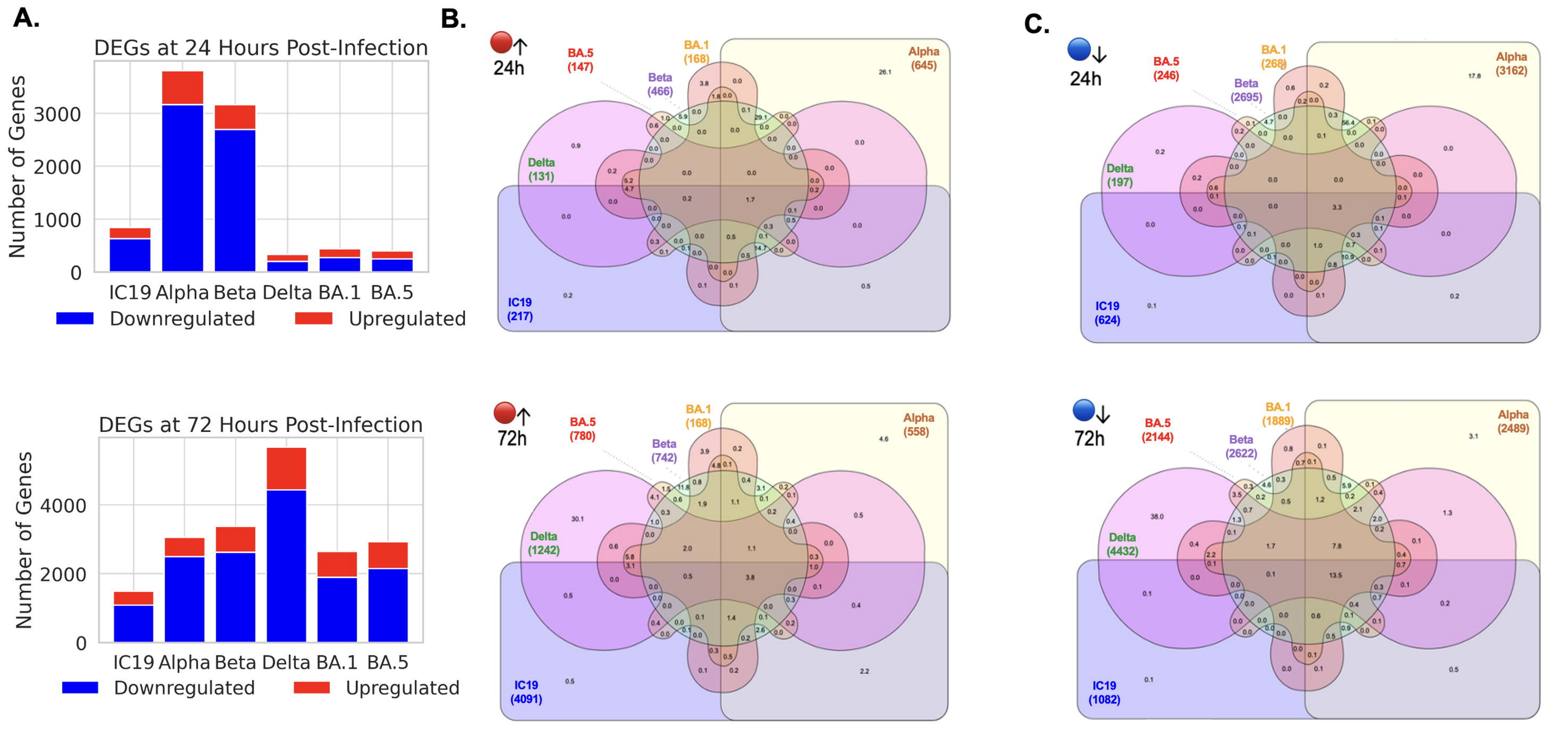
A.
DEGs at 24 Hours Post-Infection
Number of Genes
0
1000
2000
3000
IC19 Alpha Beta Delta BA.1 BA.5
Downregulated
Upregulated
DEGs at 72 Hours Post-Infection
Number of Genes
0
2000
4000
IC19 Alpha Beta Delta BA.1 BA.5
Downregulated
Upregulated
B.
24h
BA.5 (147)
BA.1 (168)
Alpha (645)
Beta (466)
Delta (131)
IC19 (217)
72h
BA.5 (780)
BA.1 (168)
Alpha (558)
Beta (742)
Delta (1242)
IC19 (4091)
C.
24h
BA.5 (246)
BA.1 (268)
Alpha (3162)
Beta (2695)
Delta (197)
IC19 (624)
72h
BA.5 (2144)
BA.1 (1889)
Alpha (2489)
Beta (2622)
Delta (4432)
IC19 (1082)

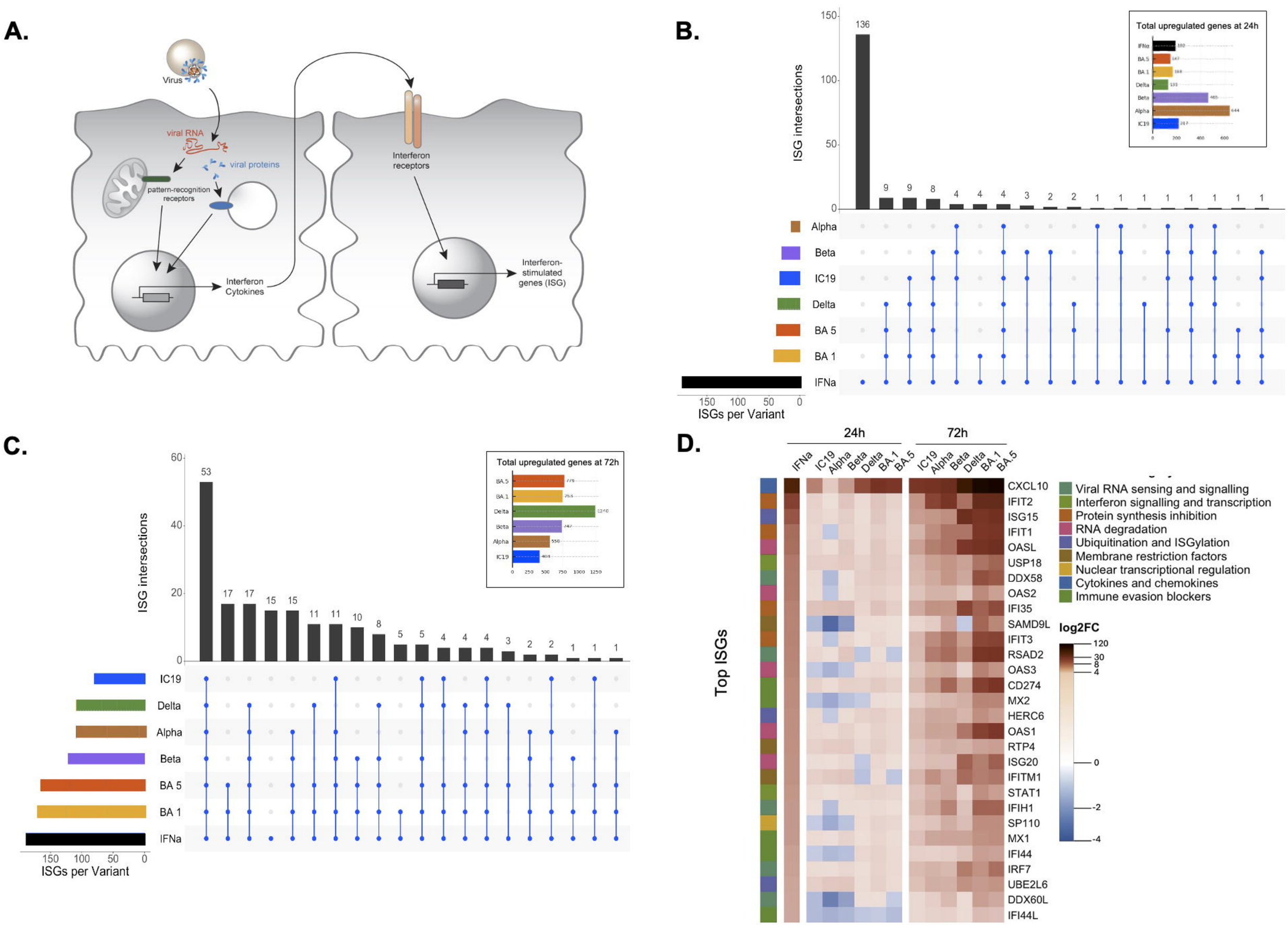
A.
Virus
viral RNA
viral proteins
pattern-recognition receptors
Interferon Cytokines
Interferon receptors
Interferon-stimulated genes (ISG)
B.
ISG intersections
Total upregulated genes at 24h
IFNa
BA.5
BA.1
Delta
Beta
Alpha
IC19
ISGs per Variant
C.
ISG intersections
Total upregulated genes at 72h
ISGs per Variant
D.
24h
72h
Top ISGs
CXCL10
IFIT2
ISG15
IFIT1
OASL
USP18
DDX58
OAS2
IFI35
SAMD9L
IFIT3
RSAD2
OAS3
CD274
MX2
HERC6
OAS1
RTP4
ISG20
IFITM1
STAT1
IFIH1
SP110
MX1
IFI44
IRF7
UBE2L6
DDX60L
IFI44L
Viral RNA sensing and signalling
Interferon signalling and transcription
Protein synthesis inhibition
RNA degradation
Ubiquitination and ISGylation
Membrane restriction factors
Nuclear transcriptional regulation
Cytokines and chemokines
Immune evasion blockers
log2FC

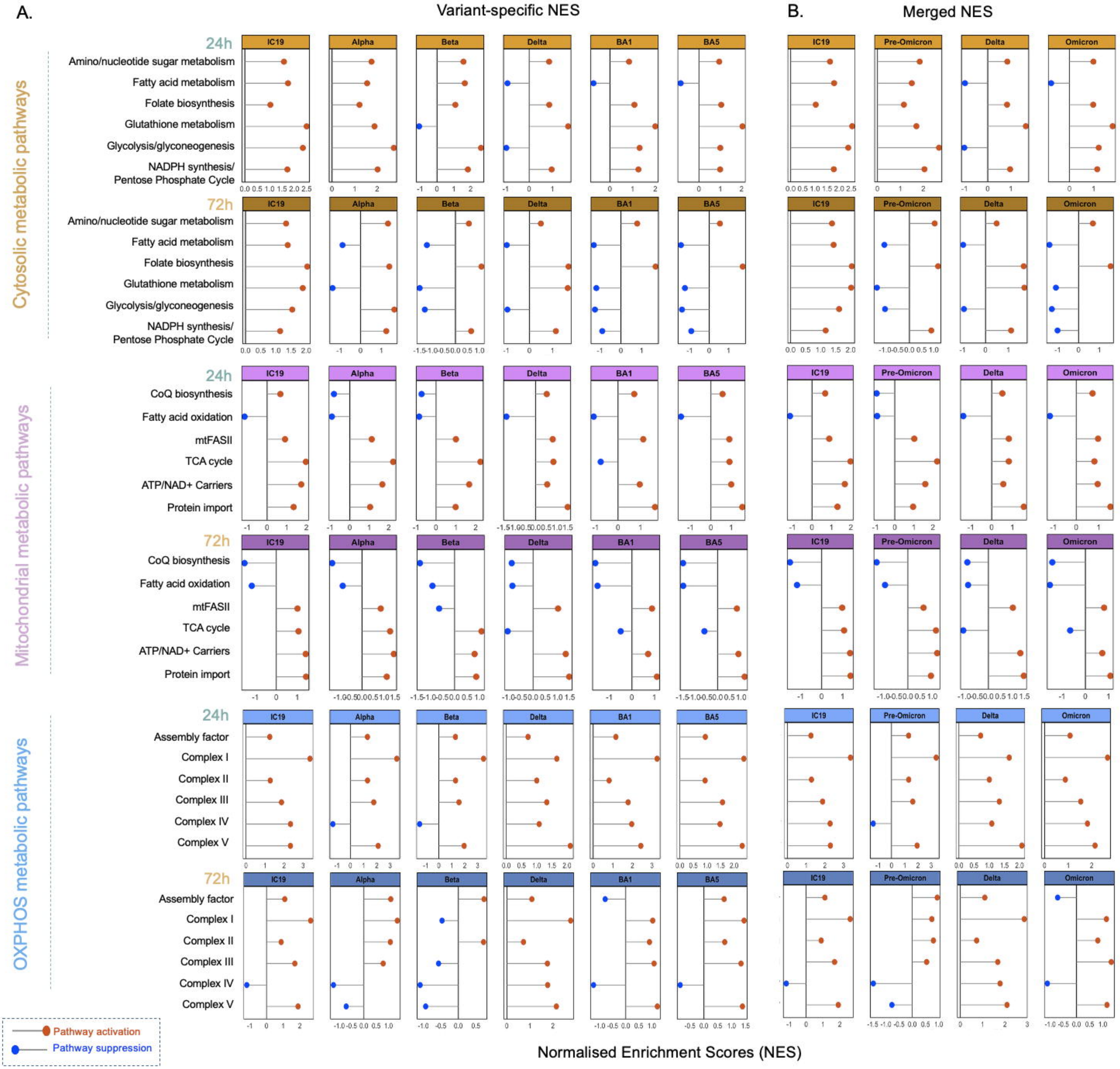
A.
Variant-specific NES
B.
Merged NES
Cytosolic metabolic pathways
24h
72h
Amino/nucleotide sugar metabolism
Fatty acid metabolism
Folate biosynthesis
Glutathione metabolism
Glycolysis/glyconeogenesis
NADPH synthesis/
Pentose Phosphate Cycle
Mitochondrial metabolic pathways
CoQ biosynthesis
Fatty acid oxidation
mtFASII
TCA cycle
ATP/NAD+ Carriers
Protein import
OXPHOS metabolic pathways
Assembly factor
Complex I
Complex II
Complex III
Complex IV
Complex V
IC19
Alpha
Beta
Delta
BA1
BA5
Pre-Omicron
Omicron
Pathway activation
Pathway suppression
Normalised Enrichment Scores (NES)

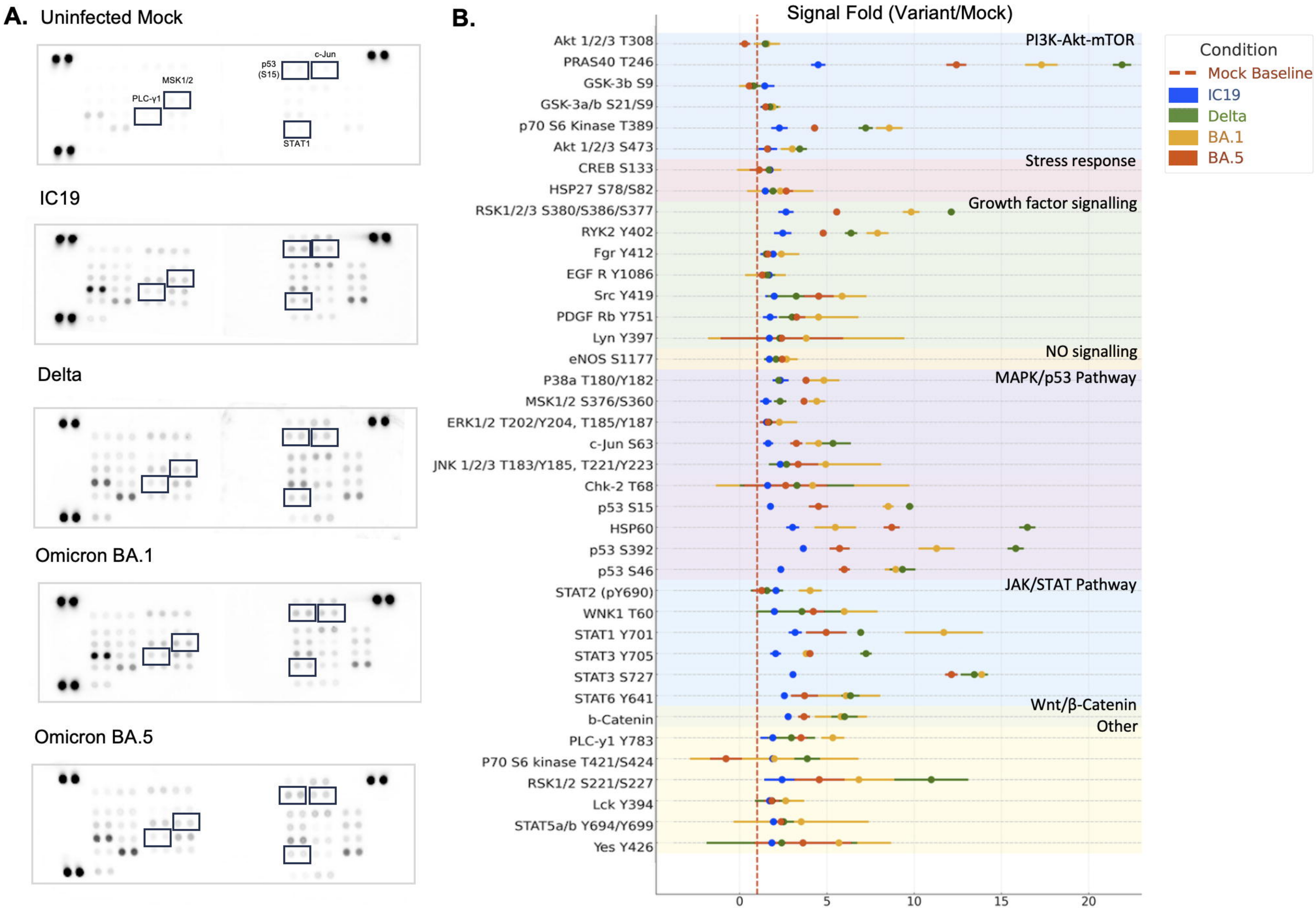
A.
Uninfected Mock
p53 (S15)
c-Jun
MSK1/2
PLC-γ1
STAT1
IC19
Delta
Omicron BA.1
Omicron BA.5
B.
Signal Fold (Variant/Mock)
Akt 1/2/3 T308
PRAS40 T246
GSK-3b S9
GSK-3a/b S21/S9
p70 S6 Kinase T389
Akt 1/2/3 S473
CREB S133
HSP27 S78/S82
RSK1/2/3 S380/S386/S377
RYK2 Y402
Fgr Y412
EGF R Y1086
Src Y419
PDGF Rb Y751
Lyn Y397
eNOS S1177
P38a T180/Y182
MSK1/2 S376/S360
ERK1/2 T202/Y204, T185/Y187
c-Jun S63
JNK 1/2/3 T183/Y185, T221/Y223
Chk-2 T68
p53 S15
HSP60
p53 S392
p53 S46
STAT2 (pY690)
WNK1 T60
STAT1 Y701
STAT3 Y705
STAT3 S727
STAT6 Y641
b-Catenin
PLC-y1 Y783
P70 S6 kinase T421/S424
RSK1/2 S221/S227
Lck Y394
STAT5a/b Y694/Y699
Yes Y426
PI3K-Akt-mTOR
Stress response
Growth factor signalling
NO signalling
MAPK/p53 Pathway
JAK/STAT Pathway
Wnt/β-Catenin
Other
0
5
10
15
20
Condition
Mock Baseline
IC19
Delta
BA.1
BA.5

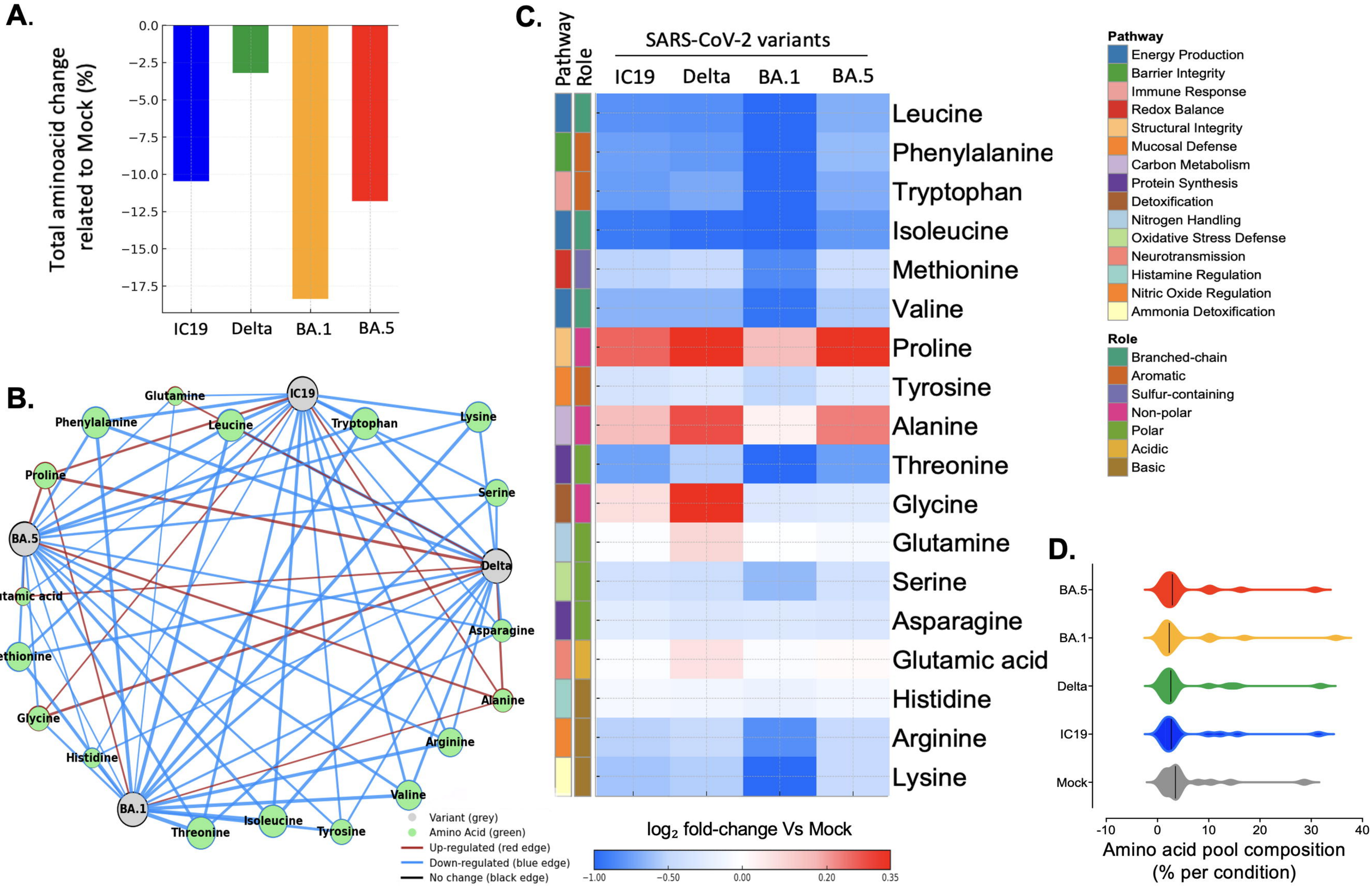
A.
Total aminoacid change related to Mock (%)
0.0
−2.5
−5.0
−7.5
−10.0
−12.5
−15.0
−17.5
IC19
Delta
BA.1
BA.5
B.
Glutamine
IC19
Phenylalanine
Leucine
Tryptophan
Lysine
Proline
Serine
BA.5
Delta
Glutamic acid
Asparagine
Methionine
Alanine
Glycine
Arginine
Histidine
Valine
BA.1
Isoleucine
Threonine
Tyrosine
Variant (grey)
Amino Acid (green)
Up-regulated (red edge)
Down-regulated (blue edge)
No change (black edge)
C.
Pathway
Role
SARS-CoV-2 variants
IC19
Delta
BA.1
BA.5
Leucine
Phenylalanine
Tryptophan
Isoleucine
Methionine
Valine
Proline
Tyrosine
Alanine
Threonine
Glycine
Glutamine
Serine
Asparagine
Glutamic acid
Histidine
Arginine
Lysine
log2 fold-change Vs Mock
−1.00
−0.50
0.00
0.20
0.35
Pathway
Energy Production
Barrier Integrity
Immune Response
Redox Balance
Structural Integrity
Mucosal Defense
Carbon Metabolism
Protein Synthesis
Detoxification
Nitrogen Handling
Oxidative Stress Defense
Neurotransmission
Histamine Regulation
Nitric Oxide Regulation
Ammonia Detoxification
Role
Branched-chain
Aromatic
Sulfur-containing
Non-polar
Polar
Acidic
Basic
D.
BA.5
BA.1
Delta
IC19
Mock
-10
0
10
20
30
40
Amino acid pool composition
(% per condition)